Nanoscale

Photothermal Behaviour of Titanium Nitride Nanoparticles Evaluated by Transient X-ray Diffraction

Journal:	*Nanoscale*
Manuscript ID	NR-ART-11-2020-008202.R1
Article Type:	Paper
Date Submitted by the Author:	29-Dec-2020
Complete List of Authors:	Diroll, Benjamin; Argonne National Laboratory, Center for Nanoscale Materials Brumberg, Alexandra; Northwestern University Leonard, Ariel; Northwestern University, Chemistry; Argonne National Laboratory, Chemical Sciences and Engineering Panuganti, Shobhana; Northwestern University Watkins, Nicolas; Northwestern University, Chemistry Cuthriell, Shelby; Northwestern University Harvey, Samantha; Northwestern University Kinigstein, Eli Diego; Argonne National Laboratory Yu, Jin; Argonne National Laboratory, Center for Nanoscale Materials Zhang, Xiaoyi; Argonne National Laboratory Kanatzidis, Mercouri; Northwestern University, Department of Chemistry Wasielewski, Michael; Northwestern University, Department of Chemistry Chen, Lin; Argonne National Laboratory Schaller, Richard; Argonne National Laboratory, Center for Nanoscale Materials

SCHOLARONE™
Manuscripts

Please do not adjust margins

ARTICLE

Photothermal Behaviour of Titanium Nitride Nanoparticles Evaluated by Transient X-ray Diffraction

Received 00th January 20xx,
Accepted 00th January 20xx

DOI: 10.1039/x0xx00000x

Benjamin T. Diroll,[a†*] Alexandra Brumberg,[b†] Ariel A. Leonard,[b,c] Shobhana Panuganti,[b] Nicolas E. Watkins,[b] Shelby A. Cuthriell,[b] Samantha M. Harvey,[b,d] Eli D. Kinigstein,[e] Jin Yu,[e] Xiaoyi Zhang,[e] Mercouri G. Kanatzidis,[b,d,f] Michael R. Wasielewski,[b,d] Lin X. Chen,[b,c,d] Richard D. Schaller[a,b,d*]

The photothermal properties of metal nitrides have recently received significant attention owing to diverse applications in solar energy conversion, photothermal therapies, photoreactions, and thermochromic windows. Here, the photothermal response of titanium nitride nanoparticles is examined using transient X-ray diffraction, in which optical excitation is synchronized with X-ray pulses to characterize dynamic changes in the TiN lattice. Photoinduced diffraction data is quantitatively analyzed to determine increases in the TiN lattice spacing, which are furthermore calibrated against static, temperature-dependent diffraction patterns of the same samples. Measurements of 20 nm and 50 nm diameter TiN nanoparticles reveal transient lattice heating from room temperature up to ~175 °C for the highest pump fluences investigated here. Increasing excitation intensity drives sublinear increases in lattice temperature, due to increased heat capacity at the higher effective temperatures achieved at higher powers. Temporal dynamics show that higher excitation intensity drives not only higher lattice temperatures, but also unexpectedly slower cooling of the TiN nanoparticles, which is attributed to heating of the solvent proximal to the nanoparticle surface.

A Introduction

Due to a combination of metallic optical properties,[1–9] mechanical hardness,[10,11] high melting points,[12–14] silicon compatibility,[15–17] and non-toxic chemistry,[18] refractory metal nitrides such as titanium nitride (TiN) are widely touted for a range of applications otherwise performed by noble metals such as silver and gold. One such area in which TiN has shown considerable promise is in applications that span photothermal therapy,[19,20] shape-memory effects,[21] thermochromic windows,[22] photoreactions,[23–26] thermophotovoltaics ,[27–32] or photodetection.[33] In particular, recent work has demonstrated that TiN shows stronger photothermal heating compared to gold, which time-resolved optical studies attribute to strong electron-phonon coupling.[28,34–37] Although many of the aforementioned applications benefit from large surface areas that are accessible with TiN nanoparticles (NPs), time-resolved studies have so far focused on bulk TiN films.[36–40] In particular, examination of the time-resolved photothermal properties of TiN NPs in a fluid environment provides a microscopic picture of heat flow relevant to photothermal applications.

In this work, we implement optical pump, X-ray diffraction probe measurements to directly measure photothermal effects on the lattice of TiN NPs dispersed in water. These transient powder X-ray diffraction or related ultrafast electron diffraction data quantify dynamics of the nuclear structure and have shown heating,[41–43] coherent phonons,[44,45] solid-solid phase transitions,[46] and disordering or melting[47,48] of NPs. Here, comparison of diffraction patterns with and without optical pumping reveals pump-induced thermal expansion of the TiN lattice without indications of disordering, such as melting, in excess of thermal motion, pointing to the high stability of this composition. A quantitative analytical framework permits measurement of lattice shifts in Δq, and static temperature-dependent powder diffraction measurements facilitate evaluation of lattice temperature change (ΔT) owing to lattice expansion. Here, we find that the TiN NP lattice heats up from room temperature to ~175 °C under the highest pump intensity illumination employed. In the regime of higher pump intensities, effective temperature increases sub-linearly, which is attributed to elevated effective heat capacity for more intense excitation. Temporal dynamics show that heat transfer from the TiN to the solvent occurs on a 0.4-1 ns time-scale, becoming slower for higher lattice temperature.

B Results and Discussion

For the studies in this work, commercial TiN NPs with nominal diameters of 20 nm and 50 nm were purchased from Plasmachem. Representative transmission electron microscopy (TEM) images of 20 nm and 50 nm TiN NPs are shown in Figures 1a and 1b. The sample sizes estimated from selected TEM imaging were 19.8 ± 2.6 nm and 46.0 ± 10.3 nm, respectively, although the samples, particularly the 50 nm sample, were polydisperse in shape, including ellipsoidal NPs

[a.] *Center for Nanoscale Materials, Argonne National Laboratory, Lemont, IL 60439*
[b.] *Department of Chemistry, Northwestern University, Evanston, IL 60208*
[c.] *Chemical Science and Engineering, Argonne National Laboratory, Lemont IL 60439*
[d.] *Institute for Sustainability and Energy at Northwestern, Northwestern University, Evanston, IL 60208*
[e.] *X-ray Sciences Division, Argonne National Laboratory, Lemont, IL 60439*
[f.] *Department of Materials Science and Engineering, Northwestern University, Evanston, IL 60208*
† These authors contributed equally.
Electronic Supplementary Information (ESI) available: Methods and additional data may be found in the ESI. See DOI: 10.1039/x0xx00000x

Please do not adjust margins

as well as faceted cubes.[49] As these size estimates are close to vendor specifications, the samples will be referred to throughout this work as 20 nm and 50 nm TiN NPs. Room temperature X-ray diffraction data in Figure 1c confirms the cubic crystal structure of the TiN NPs, which shows three prominent peaks associated with the (111), (200), and (220) reflections. The peaks observed for both samples are at slightly smaller *q* than *some* (but not all) reports of bulk TiN,[50] shown in vertical lines in Figure 1c and Figure S1, which is attributed to deviations in stoichiometry that result in slightly different TiN lattice constants.[51,52] Based upon available literature calibrations,[52] both the TiN NP samples have lattice parameters indicative of a slightly nitrogen poor composition of 48-49 % nitrogen. Scherrer analysis of the peak broadening indicates that the samples have an average crystallite size of 20.8 nm for 20 nm particles and 29.5 nm for 50 nm particles (Figure S1 and Table S1). This suggests that the 20 nm nanoparticles are typically single crystals, whereas on average 50 nm particles contain multiple crystalline domains or defects which disrupt the crystalline order within a single particle.

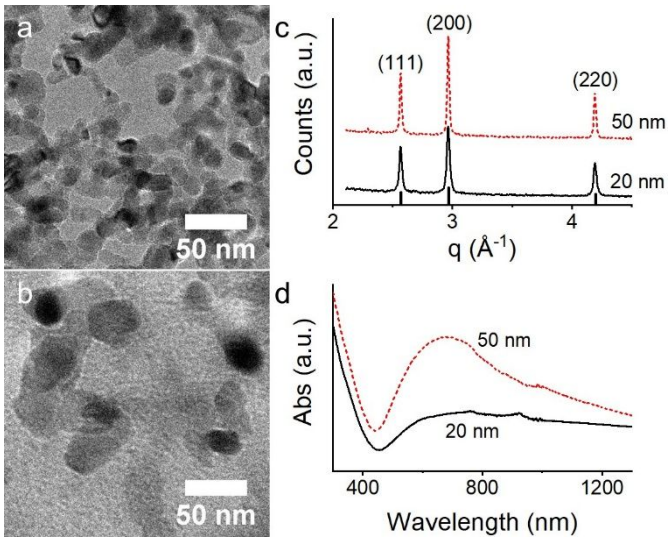

Figure 1. (a, b) Transmission electron microscopy images of (a) 20 nm TiN NPs and (b) 50 nm TiN NPs. (c) Powder X-ray diffraction of 20 nm and 50 nm TiN NPs. Cubic reflections of bulk TiN are shown in black lines.[50] (d) Visible absorption spectra of 20 nm and 50 nm TiN NPs.

Absorption spectra of the samples dispersed via sonication in water are shown in Figure 1d. As prepared, the TiN NPs have no organic coating to improve solubility. Although sedimentation of sonicated dispersions was observed over several days, this was not significant on the time-scale of the experiments reported here. Both sizes of TiN NPs showed strongly attenuated transmission at red visible wavelengths into the near infrared, attributable to absorption and scattering from localized surface plasmon resonances,[49] with a peak of transmission around 450-500 nm. The polydispersity of size and shape apparent in TEM is reflected in the broad localized surface plasmon resonances of the samples, which are substantially broader than predicted based upon an effective medium model using the properties of TiN films determined by ellipsometry.[49] In several photothermal applications, broad resonances are an advantage as they permits a large spectral range to induce nanoparticle heating. Absorption also becomes stronger at wavelengths < 450 nm due to an increased contribution from *p* to *d* interband transitions.[53–55] In this work, the samples, rapidly flowing as a jet, are optically excited on resonance with interband transitions at 400 nm for transient X-ray diffraction experiments. Previous works on the photothermal properties of plasmonic metals have shown that although all excitation wavelengths induce heating, excitation on resonance with interband transitions is more efficient for hot carrier generation than excitation resonant with intraband transitions of the electron plasma.[36,56]

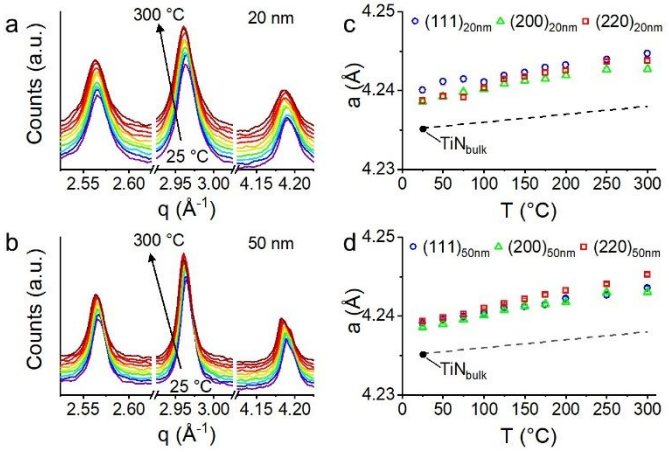

Figure 2. (a,b) Representative, static powder X-ray diffraction of (a) 20 nm and (b) 50 nm TiN NPs as a function of temperature from 25 °C to 300 °C. Data are shown in a rainbow scale from low temperature (violet) to high temperature (red). Data are offset vertically for clarity. (c, d) Cubic lattice parameter estimates based upon fitted values of the (111), (200), and (220) reflections for (c) 20 nm and (d) 50 nm TiN NPs. Dashed lines in (c, d) indicate the bulk thermal expansion of TiN.[52]

To establish a method for interpreting temperature changes in transient X-ray diffraction, temperature-dependent static X-ray diffraction data at the main cubic reflections for both TiN NP ensembles were acquired. Figures 2a and 2b show selected portions of the powder diffraction patterns of 20 nm and 50 nm TiN nanoparticles, respectively, from 25 °C to 300 °C. (Full q-range data is provided in Supplementary Information Figure S2.) As the temperature is increased up to 300 °C, peak shifts in all three reflections are observed corresponding to lattice expansion. These peak shifts can be used to develop a calibration standard for estimating temperature changes following photoexcitation *via* peak shifts in transient X-ray diffraction. Further temperature elevation near or above 350 °C, collected in air, show loss of cubic diffraction peaks and emergence of new phases (presumed to be TiO_{2-x}) as the initially dark blue TiN NP powder turns white (Figure S3).

Fitted cubic lattice parameters, *a*, estimated from the temperature-dependent peak shifts of (111), (200), and (220) reflections of the samples are shown in Figures 2c and 2d for the 20 nm and 50 nm TiN NP samples, respectively. (See Figure S4 and Table S2 for tabulated peak shifts.) The lattice expansion observed in these temperature-dependent X-ray diffraction measurements is close to linear with temperature over the range studied (up to 300 °C) yielding a fitted thermal expansion coefficient of 1.7 (± 0.3) × 10^{-5} K^{-1}, which is somewhat larger than the reported thermal expansion coefficient of 9.0 × 10^{-6} K^{-1} for bulk TiN.[52] There was no substantial difference in the behavior of the 20 nm TiN or the 50 nm TiN

This journal is © The Royal Society of Chemistry 20xx

nanoparticles with regard to lattice expansion, suggesting that both behave in a bulk-like manner.

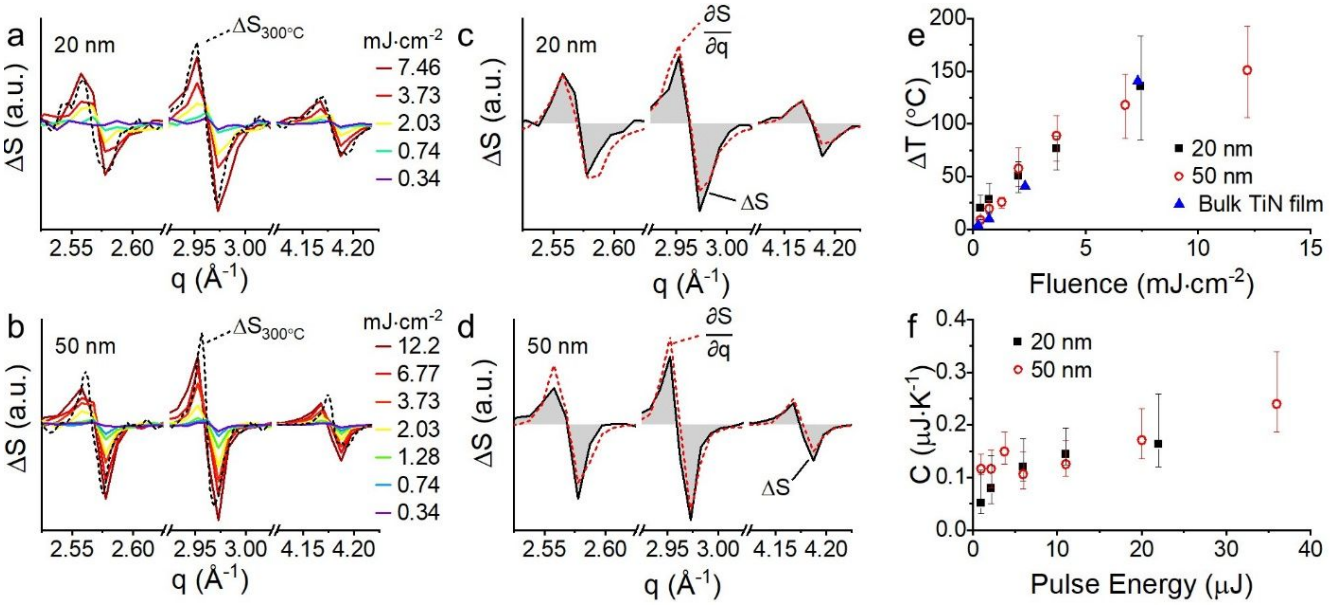

Figure 3. (a,b) Selected transient X-ray diffraction data (ΔS) for (a) 20 nm and (b) 50 nm TiN NPs for several fluences specified in the legends. All displayed data were collected at 40 ps pump-probe delay using 400 nm pump excitation. Overlaid on the transient X-ray diffraction data are dashed lines showing thermal difference diffraction curves, $\Delta S_{300°C}$, based upon temperature-dependent powder diffraction patterns at 300 °C and 25 °C. $\Delta S_{300°C}$ curves were multiplied to overlay transient X-ray diffraction data. (c, d) Selected transient X-ray diffraction data for (c) 20 nm and (d) 50 nm TiN NPs, shown with black lines. Gray shading indicate the area under the peak of ΔS. Data was acquired 40 ps after photoexcitation with 400 nm light at a fluence of 7.46 mJ·cm^{-2} for 20 nm NPs and 12.20 mJ·cm^{-2} for 50 nm NPs. The dashed red curve is the first derivative of the static scattering data before pump excitation, multiplied by Δq of -0.0011 Å^{-1} for (c) and -0.0014 Å^{-1} for (d). (e) Estimated lattice temperature change at 40 ps pump-probe delay for the 20 nm and 50 nm TiN NP samples against 400 nm excitation fluence. Estimates are calculated by averaging data from the (111), (200), and (220) reflections with error bars spanning the highest and lowest estimated values. Also shown on the plot is the change in lattice temperature reported for 400 nm excitation of bulk TiN films using transient thermoreflectance.[36] (f) Heat capacity of samples as a function of pulse energy. Estimates of heat capacity are calculated by using average, high, and low estimates of temperature change.

Transient X-ray diffraction data for the 20 nm and 50 nm TiN NPs are shown in Figure 3. Here, 1.6-ps. 400-nm pump pulses are temporally- and spatially-overlapped with probe 79-ps X-ray pulses generated from a synchrotron (the Advanced Photon Source), with a controlled pump-probe delay time. Diffraction patterns are collected both with and without the pump excitation to generate $\Delta S = S_{\text{pump on}} - S_{\text{pump off}}$. To accurately capture heating of the TiN NP lattice, data were acquired at a pump-probe delay of 40 ps, (within the instrument response function). Earlier measurements of electron-phonon coupling of bulk TiN indicate characteristic electron-phonon coupling times of *c.* 100 fs.[36,37] Therefore lattice heating is anticipated to be complete within the temporal resolution of the transient X-ray diffraction experiment. Figures 3a and 3b show typical transient X-ray diffraction data, respectively collected from the 20 and 50-nm samples, at several pump fluences for the (111), (200), and (220) reflections. Full *q*-range data shown in Figure S5 indicates that no solid-solid phase transition is observed. Overlaid in Figures 3a and 3b with black dashed lines are thermal difference diffraction data, $\Delta S_{300°C} = S_{300°C} - S_{25°C}$, based upon temperature-dependent powder diffraction patterns. In both transient X-ray diffraction patterns and thermal difference patterns, thermal expansion to larger lattice spacings produces a derivative-like feature at each individual diffraction peak comprised of increased scattering intensity at slightly smaller q ($\Delta S(q_{\text{peak}} + dq)$>0) and decreased scattering intensity at slightly larger q ($\Delta S(q_{\text{peak}} + dq)$<0). The close match of the line-shape between ΔS and $\Delta S_{300°C}$ indicates that photothermal heating observed in transient X-ray diffraction experiments compares readily with equilibrium elevated-temperature lattice conditions.

Figures 3c and 3d show ΔS data from transient X-ray diffraction experiments on 20 nm and 50 nm TiN NPs overlaid with the derivative of (background-subtracted) sample diffraction without an optical pump. (Analogous data for thermal difference diffraction data is shown in Figure S6.) The derivative-like line-shape exhibited by ΔS data indicates that the diffraction patterns result from a small change in q, as $\Delta S(q) \approx -\frac{dS(q)}{dq}\Delta q$. In particular, the close matches of the derivatives of the room temperature scattering patterns to both ΔS

static thermal differenced diffraction and transient XRD indicates that neither equilibrium nor photoinduced heating include a substantial loss of order or phase transition. This distinguishes TiN from gold, for example, where the latter presents both broadening and reduction of diffraction peak intensity in addition to shifts to smaller q.[41]

The resolution of data points in the transient diffraction measurements (0.01 Å^{-1}) is larger than Δq in most instances (Figure S7), which precludes direct peak fitting of the transient X-ray diffraction peaks in a manner sufficiently sensitive to capture peak shifts accurately. To overcome this problem and estimate peak shifts for extracting effective temperatures, ΔS arising from shifted Gaussian peak features are integrated at positive and negative lobes (shown with gray shading in Figures 3c and 3d) to determine the shift in q, Δq, according to[57]

$$2fS_{peak}\Delta q = \int_{-q}^{+q} |\Delta S(q)| dq.$$

Here, S_{peak} is the peak magnitude of the background-corrected scattering peaks, $\pm q$ values are chosen to encompass the (111), (200), or (220) peaks, and f is the photoexcited fraction of the sample, which is calculated based upon the absorption of the sample at the pump wavelength. In this case, f is approximated as 0.92 for the 20 nm samples and 0.93 for the 50 nm sample, based upon the penetration depth of the beam to I_0/e^2, calculated using the sample absorption at the pump wavelength at the widest point of the jet cross-section (Figure S8 and discussion in Supplementary Information). Δq for the (111), (200), and (220) peaks of transient X-ray diffraction data shown in Figures 3a and 3b are then translated into estimates of NP lattice temperature using calibrations of $\frac{dq_{(hkl)}}{dT}$ determined from static temperature-dependent measurements. The lattice temperature changes for the 20 nm and 50 nm TiN NPs obtained in this manner are shown in Figure 3e plotted as a function of 400 nm pump fluence. An additional indication that the estimated lattice temperature changes (and f) are reasonable comes from comparison of the transient diffraction patterns (ΔS) with $-\frac{dS(q)}{dq}\Delta q$ as shown in Figures 3c and 3d. Also in Figure 3e is the reported lattice heating of a bulk TiN film estimated from optical thermoreflectance measurements, under 400 nm pump excitation.[36] These data show that increases in the lattice temperature of the 20 nm and 50 nm TiN NP samples (as well as the bulk film) are quite similar, reaching ΔT of ~150 °C (a lattice temperature of 175 °C) under the investigated conditions. It is noteworthy that this is well within the interpolation obtained from static, temperature-dependent X-ray diffraction data in Figure 2.

Lattice temperature estimates from transient diffraction in Figure 3e show a nonlinearity at higher fluence which reduces the photothermal response. If viewed as a heat capacity, or $E_{\text{pulse}}/\Delta T$, this effective heat capacity of the TiN NPs increases at higher fluence, as shown in Figure 3f. This is consistent with Debye solids and for practical applications of TiN, which has a Debye temperature near 636K, points to diminishing returns with higher fluences. In bulk TiN, the heat capacity, dominated by the lattice heat capacity, increases by 22% from 25 °C to 175 °C.[58] By comparison, the heat capacity of gold (Debye temperature of 170 K), increases by only 2% over a similar temperature range.[59] Although both electron-phonon coupling and electron temperature may change with excitation fluence, the influence of these effects are expected to be minimal for the lattice temperature estimates with a pump-probe delay of 40 ps, at which point energy absorbed by electron and lattice temperatures are equilibrated.[36,37]

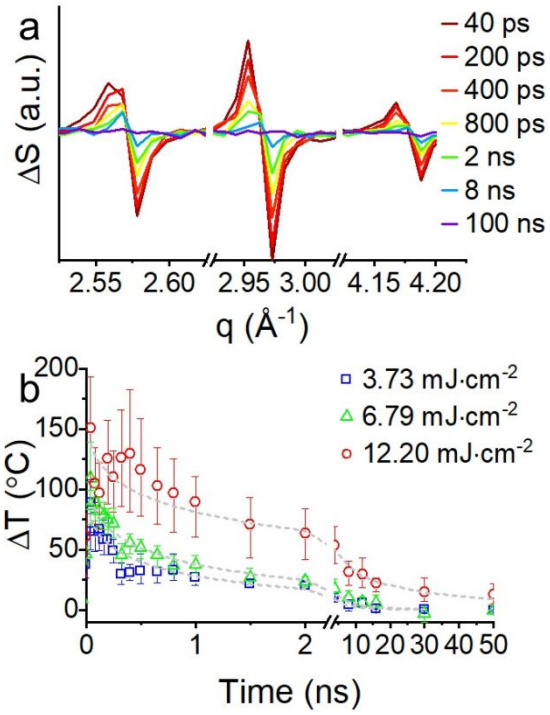

Figure 4. Transient X-ray diffraction patterns of 50 nm TiN NPs excited at a 400 nm pump fluence of 6.79 mJ·cm^{-2} for the indicated pump-probe delay times ranging from 40 ps to 100 ns. (b) Estimated temperature changes of 50 nm TiN NPs versus time for stated fluences of 400 nm pump excitation. Temperatures are estimated as described in the text with errors bars representing high and low estimates from (111), (200), and (220) peaks. Dashed gray lines show stretched exponential fits to the data.

Finally, the lattice dynamics were measured at different pump-probe delay times to observe the cooling of the hot TiN NPs. In Figure 4a, selected ΔS data are shown for 50 nm TiN NPs at a fixed pump fluence (6.79 mJ·cm^{-2}) at several different pump-probe delay times up to 100 ns. The NPs cool down following the initial optical pump pulse and the magnitude of ΔS decreases to the point at which it becomes indistinguishable from the baseline. Heat transfer from particles (subscripted p) to surrounding fluids (f) is a classical heat transfer problem in which the limiting cases are cooling dictated by either diffusion or interfacial heat transfer.[60–63] When heat transfer is limited by diffusion, the temperature decay of the particle is $\tau_D = \frac{r^2 C_p{}^2}{9 C_f \Lambda_f}$, where $\alpha_i = \Lambda_i / C_i$, Λ_i is thermal conductivity, and C_i is heat capacity. For these 50 nm TiN nanoparticles in water, the lifetime of diffusion-limited heat transfer is estimated at 400 ps. On the other hand, when heat transfer is limited by interfacial heat transfer, the decay time is $\tau_i = \frac{r C_p}{3G}$, where G is the interfacial thermal conductance. Although the interfacial thermal conductance for these particles is unknown, previous estimates of interfacially-limited thermal conductance of metallic nanoparticles in water are ~150 MW·m^{-2}·K^{-1}.[60,61,63] Using this value, the estimated heat decay time in this system is 210 ps.

To evaluate the physical processes contributing to heat transfer in these TiN NPs, Figure 4b compares the temperature relaxation for 50 nm TiN NPs excited at three different fluences. Experimentally,

This journal is © The Royal Society of Chemistry 20xx

thermal relaxation is a nonexponential processes that is slower than anticipated under either diffusion-limited or interface transfer-limited cooling, although these results are closer to the diffusion-limited case. Similar to earlier work,[41,64] dynamics are quantified in Table 1 by fitting the lattice temperature dynamics to stretched exponential decays $e^{-(t/\tau)^{\beta}}$, as depicted by the gray dashed lines in Figure 4b. At low fluence, the stretched exponential decay (510±50 ps) is longer than either analytical limit and the experimentally-observed heat dissipation of similarly sized colloidal gold NPs in water, which show a heat dissipation time constant of 380±40 ps.[64] At higher fluences, the transient X-ray diffraction dynamics appreciably slow, which is explicitly at odds with previous findings on gold NPs in water.[64] (Normalized, semi-log, and log-log data for comparison may be found in Figure S9.) In all cases, β values are smaller than previous reports on gold NPs (~0.7),[64] which implies a larger dispersion of rates in these samples. One reason for deviation from analytical models and elongation of heat dissipation times of the TiN NPs at higher fluence (or higher lattice temperature) is that heating of the fluid layer proximal to the particle surface slows heat dissipation of the particle[65] by creation of an insulating vapor layer with larger impedance mismatch with the particle than pure fluid.[66] At still higher NP temperatures, surface water may even become superheated or boil,[67,68] although the lattice temperatures estimated here are smaller than those estimated to induce boiling on a gold NP surface.[69]

Table 1. Fitting parameters for stretched exponential ($e^{-(t/\tau)^{\beta}}$) fit of fluence-dependent temperature dynamics of 50 nm TiN NPs.

Fluence (mJ/cm^2)	β	τ (ps)
3.73	0.45	510±50
6.79	0.45	720±50
12.20	0.32	1498±190

C Conclusions

In conclusion, we have shown that transient X-ray diffraction may be used to directly examine photothermal changes in the lattice temperature of TiN NPs, including for perturbations of less than 20 °C. These results show that the TiN lattice expands but does not undergo a phase transition in the regime probed, which underlines the refractory nature of the nitride metals and distinguishes them from gold NPs in photothermal applications. Under the excitation conditions used in this work, TiN NPs heat from room temperature up to as hot as 175 °C, measured by calibrating transient X-ray diffraction data against static powder diffraction measurements at elevated temperatures. The increasing heat capacity of TiN at higher temperatures leads to diminishing returns in photothermal response at the highest fluences employed here. Cooling of the heated NPs in water is a non-exponential process that appears slower than comparably sized gold NPs and unexpectedly sensitive to pump fluence. These results provide an important microscopic picture of photothermal behavior in this promising colloidal material.

Conflicts of interest

There are no conflicts to declare.

Acknowledgements

This material is based upon work supported by the National Science Foundation Graduate Research Fellowship Program under Grant No. DGE-1842165 (A.B., N.E.W., S.M.H.). This work was supported by the MSN program of the National Science Foundation (No. 1808590). This work was supported by the U.S. Department of Energy, Office of Science, Office of Basic Energy Sciences under Award DE-FG02-99ER14999 (M.R.W.). This work was performed, in part, at the Center for Nanoscale Materials, a U.S. Department of Energy Office of Science User Facility, and supported by the U.S. Department of Energy, Office of Science, under Contract No. DE-AC02-06CH11357. This research used resources of the Advanced Photon Source, a U.S. Department of Energy (DOE) Office of Science User Facility operated for the DOE Office of Science by Argonne National Laboratory under Contract No. DE-AC02-06CH11357. This work made use of the Jerome B. Cohen X-Ray Diffraction Facility supported by the MRSEC program of the National Science Foundation (DMR-1720139) at the Materials Research Center of Northwestern University and the Soft and Hybrid Nanotechnology Experimental (SHyNE) Resource (NSF ECCS-1542205).

Notes and references

1 G. V Naik, J. L. Schroeder, X. Ni, A. V. Kildishev, T. D. Sands and A. Boltasseva, *Opt. Mater. Express*, 2012, **2**, 478.
2 U. Guler, A. Boltasseva and V. M. Shalaev, *Science*, 2014, **344**, 263–264.
3 P. Patsalas and S. Logothetidis, *J. Appl. Phys.*, 2001, **90**, 4725–4734.
4 P. Patsalas, *Thin Solid Films*, 2019, **688**, 137438.
5 N. Kinsey, M. Ferrera, G. V. Naik, V. E. Babicheva, V. M. Shalaev and A. Boltasseva, *Opt. Express*, 2014, **22**, 12238.
6 S. Saha, A. Dutta, N. Kinsey, A. V. Kildishev, V. M. Shalaev and A. Boltasseva, *ACS Photonics*, 2018, **5**, 4423–4431.
7 A. S. Roberts, M. Chirumamilla, D. Wang, L. An, K. Pedersen, N. A. Mortensen and S. I. Bozhevolnyi, *Opt. Mater. Express*, 2018, **8**, 3717.
8 Y.-J. Lu, R. Sokhoyan, W.-H. Cheng, G. Kafaie Shirmanesh, A. R. Davoyan, R. A. Pala, K. Thyagarajan and H. A. Atwater, *Nat. Commun.*, 2017, **8**, 1631.
9 Y. Wang, A. Capretti and L. Dal Negro, *Opt. Mater. Express*, 2015, **5**, 2415.
10 J. -E. Sundgren and H. T. G. Hentzell, *J. Vac. Sci. Technol. A*, 1986, **4**, 2259–2279.
11 H. Holleck, *J. Vac. Sci. Technol. A Vacuum, Surfaces, Film.*, 1986, **4**, 2661–2669.
12 H. Reddy, U. Guler, Z. Kudyshev, A. V. Kildishev, V. M. Shalaev and A. Boltasseva, *ACS Photonics*, 2017, **4**, 1413–1420.
13 S. Tripura Sundari, R. Ramaseshan, F. Jose, S. Dash and A. K. Tyagi, *J. Appl. Phys.*, 2014, **115**, 033516.

14 J. A. Briggs, G. V. Naik, Y. Zhao, T. A. Petach, K. Sahasrabuddhe, D. Goldhaber-Gordon, N. A. Melosh and J. A. Dionne, *Appl. Phys. Lett.*, 2017, **110**, 101901.

15 Dae-Gyu Park, Tae-Ho Cha, Kwan-Yong Lim, Heung-Jae Cho, Tae-Kyun Kim, Se-Aug Jang, You-Seok Suh, Veena Misra, In-Seok Yeo, Jae-Sung Roh, Jin Won Park and Hee-Koo Yoon, in *International Electron Devices Meeting. Technical Digest (Cat. No.01CH37224)*, IEEE, 2001, pp. 30.6.1-30.6.4.

16 J. A. Briggs, G. V. Naik, T. A. Petach, B. K. Baum, D. Goldhaber-Gordon and J. A. Dionne, *Appl. Phys. Lett.*, 2016, **108**, 051110.

17 M. Wittmer, *J. Vac. Sci. Technol. A Vacuum, Surfaces, Film.*, 1985, **3**, 1797–1803.

18 I. Dion, C. Baquey, B. Candelon and J. R. Monties, *Int. J. Artif. Organs*, 1992, **15**, 617–621.

19 X. H. Huang, I. H. El-Sayed, W. Qian and M. A. El-Sayed, *J. Am. Chem. Soc.*, 2006, **128**, 2115–2120.

20 X. Huang, P. K. Jain, I. H. El-Sayed and M. A. El-Sayed, *Lasers Med. Sci.*, 2008, **23**, 217–228.

21 S. Ishii, K. Uto, E. Niiyama, M. Ebara and T. Nagao, *ACS Appl. Mater. Interfaces*, 2016, **8**, 5634–5640.

22 Q. Hao, W. Li, H. Xu, J. Wang, Y. Yin, H. Wang, L. Ma, F. Ma, X. Jiang, O. G. Schmidt and P. K. Chu, *Adv. Mater.*, 2018, **30**, 1705421.

23 B. Doiron, Y. Li, A. Mihai, R. Bower, N. M. Alford, P. K. Petrov, S. A. Maier and R. F. Oulton, *J. Phys. Chem. C*, 2019, **123**, 18521–18527.

24 A. Naldoni, U. Guler, Z. Wang, M. Marelli, F. Malara, X. Meng, L. V. Besteiro, A. O. Govorov, A. V. Kildishev, A. Boltasseva and V. M. Shalaev, *Adv. Opt. Mater.*, 2017, **5**, 1601031.

25 E. B. Clatworthy, S. Yick, A. T. Murdock, M. C. Allison, A. Bendavid, A. F. Masters and T. Maschmeyer, *J. Phys. Chem. C*, 2019, **123**, 3740–3749.

26 A. A. Barragan, S. Hanukovich, K. Bozhilov, S. S. R. K. C. Yamijala, B. M. Wong, P. Christopher and L. Mangolini, *J. Phys. Chem. C*, 2019, **123**, 21796–21804.

27 P. Ren and X. Yang, *Sol. RRL*, 2018, **2**, 1700233.

28 S. Ishii, R. P. Sugavaneshwar and T. Nagao, *J. Phys. Chem. C*, 2016, **120**, 2343–2348.

29 M. Chirumamilla, A. Chirumamilla, Y. Yang, A. S. Roberts, P. K. Kristensen, K. Chaudhuri, A. Boltasseva, D. S. Sutherland, S. I. Bozhevolnyi and K. Pedersen, *Adv. Opt. Mater.*, 2017, **5**, 1700552.

30 M. Kaur, S. Ishii, S. L. Shinde and T. Nagao, *Adv. Sustain. Syst.*, 2019, **3**, 1800112.

31 S. Ishii, S. L. Shinde and T. Nagao, in *Nanophotonic Materials XIV*, eds. S. Cabrini, G. Lérondel, A. M. Schwartzberg and T. Mokari, SPIE, 2017, vol. 1034404, p. 3.

32 A. Lalisse, G. Tessier, J. Plain and G. Baffou, *Sci. Rep.*, 2016, **6**, 38647.

33 S. Ishii, S. L. Shinde, W. Jevasuwan, N. Fukata and T. Nagao, *ACS Photonics*, 2016, **3**, 1552–1557.

34 U. Guler, J. C. Ndukaife, G. V. Naik, A. G. A. Nnanna, A. V. Kildishev, V. M. Shalaev and A. Boltasseva, *Nano Lett.*, 2013, **13**, 6078–6083.

35 R. A. Karaballi, Y. Esfahani Monfared and M. Dasog, *Langmuir*, 2020, **36**, 5058–5064.

36 B. T. Diroll, S. Saha, V. M. Shalaev, A. Boltasseva and R. D. Schaller, *Adv. Opt. Mater.*, 2020, **2000652**, 2000652.

37 H. George, J. Reed, M. Ferdinandus, C. DeVault, A. Lagutchev, A. Urbas, T. B. Norris, V. M. Shalaev, A. Boltasseva and N. Kinsey, *Opt. Mater. Express*, 2019, **9**, 3911.

38 B. Doiron, Y. Li, A. P. Mihai, L. F. Cohen, P. K. Petrov, N. M. Alford, R. F. Oulton and S. A. Maier, in *Plasmonics: Design, Materials, Fabrication, Characterization, and Applications XV*, eds. T. Tanaka and D. P. Tsai, SPIE, 2017, vol. 1034604, p. 3.

39 H. Ferguson, U. Guler, N. Kinsey, V. M. Shalaev, T. Norris and A. Boltasseva, in *Conference on Lasers and Electro-Optics*, OSA, Washington, D.C., 2017, p. JTh2A.22.

40 H. Ferguson, U. Guler, N. Kinsey, V. M. Shalaev, T. Norris and A. Boltasseva, in *Conference on Lasers and Electro-Optics*, OSA, Washington, D.C., 2016, vol. 50, p. FF2D.1.

41 A. Plech, V. Kotaidis, S. Grésillon, C. Dahmen and G. von Plessen, *Phys. Rev. B*, 2004, **70**, 195423.

42 B. Guzelturk, J. K. Utterback, I. Coropceanu, V. Kamysbayev, E. M. Janke, M. Zajac, N. Yazdani, B. L. Cotts, S. Park, A. Sood, M. F. Lin, A. H. Reid, M. E. Kozina, X. Shen, S. P. Weathersby, V. Wood, A. Salleo, X. Wang, D. V. Talapin, N. S. Ginsberg and A. M. Lindenberg, *ACS Nano*, 2020, **14**, 4792–4804.

43 T. Vasileiadis, L. Waldecker, D. Foster, A. Da Silva, D. Zahn, R. Bertoni, R. E. Palmer and R. Ernstorfer, *ACS Nano*, 2018, **12**, 7710–7720.

44 J. N. Clark, L. Beitra, G. Xiong, A. Higginbotham, D. M. Fritz, H. T. Lemke, D. Zhu, M. Chollet, G. J. Williams, M. Messerschmidt, B. Abbey, R. J. Harder, A. M. Korsunsky, J. S. Wark and I. K. Robinson, *Science (80-.).*, 2013, **341**, 56–59.

45 G. M. Vanacore, J. Hu, W. Liang, S. Bietti, S. Sanguinetti and A. H. Zewail, *Nano Lett.*, 2014, **14**, 6148–6154.

46 M. S. Kirschner, B. T. Diroll, P. Guo, S. M. Harvey, W. Helweh, N. C. Flanders, A. Brumberg, N. E. Watkins, A. A. Leonard, A. M. Evans, M. R. Wasielewski, W. R. Dichtel, X. Zhang, L. X. Chen and R. D. Schaller, *Nat. Commun.*, 2019, **10**, 1–8.

47 M. S. Kirschner, D. C. Hannah, B. T. Diroll, X. Zhang, M. J. Wagner, D. Hayes, A. Y. Chang, C. E. Rowland, C. M. Lethiec, G. C. Schatz, L. X. Chen and R. D. Schaller, *Nano Lett.*, 2017, **17**, 5314–5320.

48 G. F. Mancini, T. Latychevskaia, F. Pennacchio, J. Reguera, F. Stellacci and F. Carbone, *Nano Lett.*, 2016, **16**, 2705–2713.

49 U. Guler, S. Suslov, A. V. Kildishev, A. Boltasseva and V. M. Shalaev, *Nanophotonics*, 2015, **4**, 269–276.

50 R. W. G. Wyckoff, *Crystal Structures*, Interscience Publishers, New York, 2nd edn., 1963.

51 V. Valvoda, R. Kužel, R. Černý and L. Dobiášová, *Mater. Sci. Eng.*, 1988, **104**, 223–234.

52 K. Aigner, W. Lengauer, D. Rafaja and P. Ettmayer, *J. Alloys Compd.*, 1994, **215**, 121–126.

This journal is © The Royal Society of Chemistry 20xx

53 J. Rivory, J. M. Behaghel, S. Berthier and J. Lafait, *Thin Solid Films*, 1981, **78**, 161–165.
54 A. Schlegel, P. Wachter, J. J. Nickl and H. Lingg, *J. Phys. C Solid State Phys.*, 1977, **10**, 4889–4896.
55 B. Karlsson, R. P. Shimshock, B. O. Seraphin and J. C. Haygarth, *Sol. Energy Mater.*, 1983, **7**, 401–411.
56 E. Minutella, F. Schulz and H. Lange, *J. Phys. Chem. Lett.*, 2017, **8**, 4925–4929.
57 E. J. Sie, J. W. McLver, Y. H. Lee, L. Fu, J. Kong and N. Gedik, *Nat. Mater.*, 2015, **14**, 290–294.
58 M. W. Chase, Ed., *NIST-JANAF Thermochemical Tables*, AIP Publishing, New York, 1998.
59 Y. Takahashi and H. Akiyama, *Thermochim. Acta*, 1986, **109**, 105–109.
60 G. V Hartland, *Chem. Rev.*, 2011, **111**, 3858–3887.
61 O. M. Wilson, X. Hu, D. G. Cahill and P. V. Braun, *Phys. Rev. B*, 2002, **66**, 224301.
62 Z. Ge, D. G. Cahill and P. V. Braun, *Phys. Rev. Lett.*, 2006, **96**, 1–4.
63 Z. Ge, D. G. Cahill and P. V. Braun, *J. Phys. Chem. B*, 2004, **108**, 18870–18875.
64 M. Hu and G. V. Hartland, *J. Phys. Chem. B*, 2002, **106**, 7029–7033.
65 S. Merabia, S. Shenogin, L. Joly, P. Keblinski and J. L. Barrat, *Proc. Natl. Acad. Sci. U. S. A.*, 2009, **106**, 15113–15118.
66 E. Sassaroli, K. C. P. Li and B. E. O'Neill, *Phys. Med. Biol.*, 2009, **54**, 5541–5560.
67 Y. Dou, L. V. Zhigilei, N. Winograd and B. J. Garrison, *J. Phys. Chem. A*, 2001, **105**, 2748–2755.
68 V. Kotaidis, C. Dahmen, G. Von Plessen, F. Springer and A. Plech, *J. Chem. Phys.*, , DOI:10.1063/1.2187476.
69 M. Hu, H. Petrova and G. V. Hartland, *Chem. Phys. Lett.*, 2004, **391**, 220–225.

This journal is © The Royal Society of Chemistry 20xx

The submitted manuscript has been created by UChicago Argonne, LLC, Operator of Argonne National Laboratory ("Argonne"). Argonne, a U.S. Department of Energy Office of Science laboratory, is operated under Contract No. DE-AC02-06CH11357. The U.S. Government retains for itself, and others acting on its behalf, a paid-up nonexclusive, irrevocable worldwide license in said article to reproduce, prepare derivative works, distribute copies to the public, and perform publicly and display publicly, by or on behalf on the Government. The Department of Energy will provide public access to these results of federally sponsored research in accordance with the DOE Public Access Plan. http://energy.gov/downloads/doe-public-access-plan.

This journal is © The Royal Society of Chemistry 20xx